

Machine- and deep-learning-driven angular momentum inference from BHEX observations of the $n = 1$ photon ring

JOSEPH FARAH,^{1,2} JORDY DAVELAAR,^{3,4,5,6} DANIEL PALUMBO,^{7,8} MICHAEL JOHNSON,^{7,8} AND JONATHAN DELGADO⁹

¹*Las Cumbres Observatory, 6740 Cortona Drive, Suite 102, Goleta, CA 93117-5575, USA*

²*Department of Physics, University of California, Santa Barbara, CA 93106-9530, USA*

³*Department of Astrophysical Sciences, Peyton Hall, Princeton University, Princeton, NJ 08544, USA*

⁴*NASA Hubble Fellowship Program, Einstein Fellow*

⁵*Center for Computational Astrophysics, Flatiron Institute, 162 Fifth Avenue, New York, NY 10010, USA*

⁶*Department of Astronomy and Columbia Astrophysics Laboratory, Columbia University, 550 W 120th St, New York, NY 10027, USA*

⁷*Center for Astrophysics — Harvard & Smithsonian, 60 Garden Street, Cambridge, MA 02138, USA*

⁸*Black Hole Initiative at Harvard University, 20 Garden Street, Cambridge, MA 02138, USA*

⁹*Department of Mathematics, University of California, Irvine, CA 92697, USA*

ABSTRACT

The $n = 1$ photon ring is an important probe of black hole (BH) properties and will be resolved by the Black Hole Explorer (BHEX) for the first time. However, extraction of black hole parameters from observations of the $n = 1$ subring is not trivial. Developing this capability can be achieved by building a sample of $n = 1$ subring simulations, as well as by performing feature extraction on this high-volume sample to track changes in the geometry, which presents significant computational challenges. Here, we present a framework for the study of $n = 1$ photon ring behavior and BH property measurement from BHEX images. We use `KerrBAM` to generate a grid of $\gtrsim 10^6$ images of $n = 1$ photon rings spanning the entire space of Kerr BH spins and inclinations. Intensity profiles are extracted from images using a novel feature extraction method developed specifically for BHEX. This novel method is highly optimized and outperforms existing EHT methods by a factor of ~ 3000 . Additionally, we propose a novel, minimal set of geometric measurables for characterizing the behavior of the $n = 1$ subring geometry. We apply these measurables to our simulation grid and test spin recovery on simulated images using: (i) gradient boosting, a machine learning algorithm; and (ii) an extension of Deep Horizon, a deep learning framework. We find $\gtrsim 90\%$ correct recovery of BH properties using the machine/deep learning approaches, and characterize the space of resolution-dependent geometric degeneracies. Finally, we test both approaches on GRMHD simulations of black hole accretion flows, and report accurate recovery of spin at the expected inclination of M87*.

Keywords: Galaxy: lorem-ipsu

1. INTRODUCTION

In April 2019, the Event Horizon Telescope (EHT) Collaboration published the first image of a black hole (Event Horizon Telescope Collaboration et al. 2019a,b), representing a significant step forward in resolving and imaging astrophysical phenomena via very-long-baseline interferometry (VLBI). The unprecedented resolution of the image ($\approx 20 \mu\text{as}$) uniquely probed event-horizon scale phenomena and directly facilitated the strongest tests of general relativity to-date (e.g., Event Horizon Telescope Collaboration et al. 2019e; Event Horizon Telescope Collaboration 2021a; Bambi et al. 2019; Psaltis 2019; etc.). However, while this remarkable resolution was sufficient to probe the shadows of the M87* and Sgr A* black holes (Event Horizon Telescope Collabora-

tion et al. 2022a,b), it was still inadequate to probe the more complex features of event-horizon scale emission predicted by theory, such as the photon ring. Recently, a space-baseline extension to the EHT (the Black Hole Explorer; BHEX) has been proposed to overcome these limitations and help resolve open questions about general relativity and other fundamental physics (Johnson et al. 2024; Akiyama et al. 2024).

In particular, the higher resolution of BHEX will enable direct observation and study of a black hole’s photon ring (Lupsasca et al. 2024b), a shell of unstable photon orbits which, in aggregate, produce a sharp emission feature on the gravitationally lensed image of the black hole seen by a distant observer. The photons completing n half-orbits around the black hole produce n distinct and nested subrings (Johnson et al. 2020). Of these subrings, the $n = 0$ direct image is primarily determined by the fluid flow and only partially determined by the spacetime. By contrast, the morphology of the $n \geq 1$ subrings (the “photon rings”) is only dictated

by unstable photon orbits and are therefore mostly dependent on the properties of the black hole spacetime (e.g., spin, inclination relative to the observer, etc.) (e.g., Broderick et al. 2022). The resolution of BHEX is expected to be sufficient to probe at least the $n = 1$ subring, thus enabling direct and precise measurements of black hole properties, particularly spin (Johnson et al. 2020).

The behavior of the $n = 1$ photon ring as modified by spin is poorly understood, presenting a potential hurdle for precision measurements via BHEX observations (see e.g., Lupsasca et al. 2024a; for a review). Unlike the critical curve, which shows substantial deviation from circularity at edge-on inclination and spins approaching unity (e.g., Bardeen 1973; de Vries 2003; Cunha & Herdeiro 2018; Farah et al. 2020; Gralla et al. 2020; etc), the equivalent modification to the $n = 1$ subring is more complex and more subtle. Previous studies have characterized the overall size and ellipticity (Broderick et al. 2022; Pagnat et al. 2022; Gralla 2020), which varies with the angular momentum of the black hole. The azimuthal brightness modulation of the $n = 1$ subring, which can be modeled by a shape known as an m -ring (Johnson et al. 2020), also varies with spin. The precise relationship between these quantities and the properties of the black hole is still unknown; however, characterizing these relationships is essential for measurements with detections of the first subring.

The limited ability to observe such objects in nature results in a heavy reliance on simulations (e.g., Event Horizon Telescope Collaboration et al. 2019d,e, 2022c,d), which are computationally challenging to perform with existing tools. In particular, in order to study the $n = 1$ subring properties, we rely on computational methods such as general relativistic magnetohydrodynamic (GRMHD) simulations, which are computationally expensive to perform for the full parameter space in e.g. spin. In addition, image feature extraction tools developed for EHT applications involving a small number of images are robust but have generally poor scalability, requiring weeks or even months to analyze the large ($\gtrsim 10^5$) number of images needed for machine-learning-enabled analyses.

In this paper, we present a novel framework to enable large-scale studies of the $n = 1$ photon subring. We exploit the fast semi-analytic simulation software KerrBAM (Palumbo et al. 2022) to simulate the first subring and develop bespoke tools to perform analyses on feasible timescales. In Section 2, we describe the efficient generation of a suite of $n = 1$ photon rings spanning all possible spins and inclinations using KerrBAM, a recently-developed semi-analytic accretion modeling code. In Section 3, we introduce and evaluate “recursive brightest-point extraction”, a novel feature extraction approach designed specifically for BHEX and built to be thousands of times more computationally efficient than existing tools. In Section 4, we introduce a set of non-redundant geometric observables which can characterize the shape and emission characteristics of the various subrings in our simulation grid. We use these geometric observables to provide the first numerical analysis of the behavior of the $n = 1$ subring across the Kerr parameter space of spins and inclinations. In Section 5 we demonstrate the ability of these observables

as an unambiguous measurement tool by training machine- and deep-learning algorithms to estimate black hole properties from both numerical observables as well as full images of subrings simulated with KerrBAM. Finally, in Section 6 we directly apply our methods to GRMHD-simulated black holes. We summarize our conclusions and outlook for BHEX measurements in Section 7.

2. SIMULATION GENERATION VIA KerrBAM

The inaccessibility of the $n = 1$ photon ring given current observational limitations results in our understanding being theoretical and largely simulation-based (e.g., Event Horizon Telescope Collaboration et al. 2019d,e, 2022c,d). Machine learning algorithms in particular benefit from large datasets to improve performance, particularly when generalizing training features to real-world behavior or attempting to recover numerical quantities in a continuous fashion (Hastie 2009). Full GRMHD simulations, while frequently used and closer to reality than semi-analytic simulations, are also computationally expensive to generate, presenting an early bottleneck in attempts to characterize subtle feature behavior. Fortunately, recent years has seen the development of new models and techniques for analytic or semi-analytic computation and/or approximation of black hole accretion flows, which have come with a substantial increase in performance (Gelles et al. 2021; Palumbo et al. 2022; Cárdenas-Avendaño et al. 2023).

We generated a simulated dataset of 10^6 images to use for training. This is a substantial (10x) increase in dataset size as compared to previous similar analyses (e.g., Deep Horizon: van der Gucht et al. 2020). The dataset size is motivated by the subtlety of the subring behavior we hope to capture; the spin and inclination parameter space has steep gradients (particularly towards maximal spin or edge-on inclination) which require dense sampling to characterize. The simulated images are generated with the KerrBAM simulator, a semi-analytic ray tracing engine capable of producing images of all $n \geq 0$ subrings (Palumbo et al. 2022). We fixed all accretion flow parameters to standard values following Palumbo et al. (2022). For the parameters controlling the black hole spacetime, we fixed all parameters to values consistent with known values for M87*, with the exception of angular momentum (spin) a , inclination θ_0 , and emission radius. The fixed values are summarized in Table 1. Spin was varied between almost minimal ($|a| = 0.04$, in units of Jc/M^2 , where J is the angular momentum of the black hole) and almost maximal ($|a| = 0.94$) for both negative (spin axis oriented away from observer) and positive (spin axis oriented towards observer) spin. Inclination was varied between face-on ($\theta_0 = 0^\circ$, parallel to the spin axis) and near-edge-on ($\theta_0 = 85^\circ$, almost perpendicular to the spin axis). The emission radius was varied between $3M$ (where M is equivalent to the Schwarzschild radius of the black hole via $M \sim r_s c^2 / 2G$) and $7M$. Images were generated with adaptive ray tracing enabled and resized to a field-of-view (FOV) of $80 \mu\text{as}$ and resolution 128×128 pixels using a linear spline interpolation.

A sample set of images from the dataset are shown in Figure 1. These images show the varying behavior of the

Parameter	FOV ^a	M^b	D^c	PA ^d
Value	80 μ as	$6.5 \times 10^9 M_\odot$	5.1×10^{23} m	0°

^aThe field-of-view of the output image.

^bThe mass of the simulated black hole, set to the M87* mass.

^cThe distance between the observer and the simulated black hole, set to the M87* distance.

^dThe position angle of the spin axis projected in the observer plane, corresponding to a rotation of the image.

Table 1. KerrBAM simulation parameters controlling the black hole spacetime. We cite [Event Horizon Telescope Collaboration et al. \(2019c\)](#) where needed for relevant values.

$n = 1$ photon ring the $n = 1$ photon ring for varying black hole parameters. At edge-on inclination, the brightness and circular asymmetry becomes more pronounced at higher spin. However, at face-on inclinations, this behavior is significantly less prominent. The variation in spin at these low inclinations is more apparent as a change in the brightness modulation around the ring.

3. RECURSIVE BRIGHTEST-POINT EXTRACTION

For this analysis, we seek to quantify the emission profile and shape of the $n = 1$ subring, in order to assess how it varies with spin. Image-domain, ring-based feature extraction has been developed for previous VLBI imaging analyses and has enabled, among other things, size and mass measurements of the M87* black hole based on images of the shadow ([Johannsen et al. 2016](#); [Chael 2024](#)). Once a series of points corresponding to the brightness profile has been measured, Bayesian inference methods can be used to quantify the geometry of the ring shape. By quantifying the modification of the shape with spin and inclination, we can make assessments about the feasibility of using the subring shape to recover black hole parameters in data taken by BHEX.

The most common method for extracting a ring-like brightness profile involves identifying peak points of flux along rays emanating in all directions from an assumed center. This method was used to make measurements of the black hole shadows of M87* and Sgr A* ([Event Horizon Telescope Collaboration et al. 2019c, 2022b](#)). In some implementations, the assumed center is fixed and is not recalculated; however, in others, the assumed center is recalculated afterwards to minimize the average peak distance from the center. We use the ray-based feature extraction implementation in `eht-imaging`, specifically the REX module, to test the performance and efficiency of ray-based feature extraction ([Chael 2024](#)). We find in practice that ray-based feature extraction has several limitations that present potential obstacles to our analysis. First, due to the need to scan along dozens of rays and perform several objective function minimizations, this method of feature extraction is slow, with peak flux extractions ranging from ≈ 1 –10 seconds. This time range would result in a required time budget of ≈ 10 –100 days to fully analyze our 10^6 simulated images. Additionally, the method is

somewhat dependent on the assumption of circularity, which is not consistently met by images of the $n = 1$ subring. Particularly at high spin, the shape may be significantly asymmetrical in both brightness distribution and ellipticity, resulting in incorrect or incomplete extractions.

To address these limitations, we have developed a novel and bespoke method of feature extraction designed for maximum robustness and performance specifically on BHEX subring images. The new algorithm distills the process of extracting peak fluxes into two vectorized steps which are then applied recursively. Given a BHEX image $I(x, y)$ of a photon subring with emission following some arbitrary parameterized curve $C(t)$, a characteristic angular radius \mathcal{R} , an intensity threshold τ , and an initially empty list of emission profile points $\{\mathcal{L}\}$, the algorithm is as follows:

1. Identify the brightest point (x_B, y_B) in the image based on intensity $I(x, y)$.
 - (a) IF $I(x_B, y_B) \leq \tau$: this is considered noise. QUIT and RETURN the list of points $\{\mathcal{L}\}$ corresponding to the emission profile.
 - (b) IF $I > \tau$: The coordinate (x_B, y_B) is considered a peak flux location; ADD to the list $\{\mathcal{L}\}$ corresponding to the emission profile of the image.
2. Mask out a circular region of radius \mathcal{R} and center (x_B, y_B) in the image.
3. RETURN the masked image, the updated list of points $\{\mathcal{L}\}$, the radius \mathcal{R} , and the threshold τ to the function recursively.

A visualization of this algorithm is shown in [Figure 2](#). The masking radius \mathcal{R} is chosen based on the estimated width α of the emission profile; a choice of $\mathcal{R} < \alpha$ may result in an incorrect recovery. When $\mathcal{R} \geq \alpha$, \mathcal{R} controls the density of the points recovered along the ring. For an emission profile total integrated length $\ell = \int_C dt$, the number of points N produced with a chosen $\mathcal{R} \geq \alpha$ will be, on average, $N \sim \ell/\mathcal{R}$. The choice of τ is more complex but simultaneously less impactful; an optimal choice would be slightly lower than the dimmest point on the desired emission curve, but this is difficult to ascertain prior to calculating the emission profile. Another natural choice is simply an estimate of the average background intensity, which is straightforward to calculate quickly. As the emission profile is repeatedly masked out by step (2) in the algorithm, leaving only the background, the average background intensity served as an effective stopping criterion in our testing.

We implement our novel recursive brightest-point (RBP) extraction algorithm in `python` using vectorized tools in the `scipy` scientific computing package and compare performance to REX. The short, recursive nature of the RBP algorithm, combined with the full vectorization, results in a speed increase of ≈ 1 –3 $\times 10^3$ x over ray-based feature extraction. On average, the RBP algorithm takes $\sim 10^{-3}$ seconds per extraction, compared to ≈ 1 second for REX. The spread in

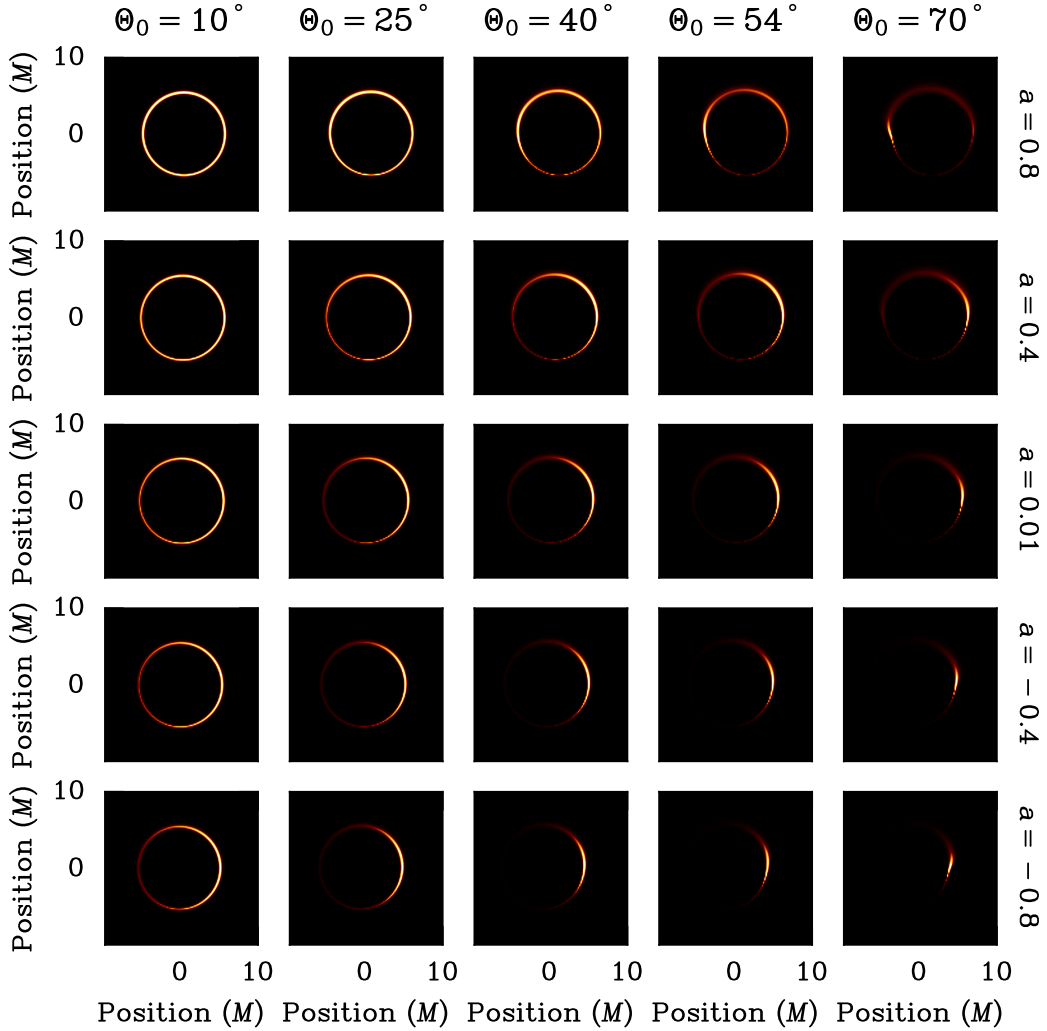


Figure 1. Sampled $n = 1$ photon rings generated with KerrBAM. Our dataset consists of $\gtrsim 10^6$ images spanning almost the entire Kerr parameter space.

this extraction time for RBP is also small, as the performance of RBP is completely unaffected by the geometry of the image ($\sim 1 \times 10^{-4}$). By contrast, REX tends to perform worse (both in terms of time complexity and extraction success) on images with higher spins and inclinations, as the image becomes less circular and the azimuthal modulation of the brightness becomes more asymmetric.

However, RBP is strongly sensitive to the assumption that the brightest points in the image lie on the $n = 1$ subring. Other emission present—for example, in an aggregate image containing all subrings—will cause incorrect extractions using RBP. By contrast, REX scans for the brightest point along a particular ray, which the $n = 1$ subring emission will frequently satisfy. In practice, RBP is useful for developing large training sets on clean images where speed is a priority, while REX is better suited for more complex individual cases (e.g., real image reconstructions), where the time budget is greater but greater robustness is desired.

4. GEOMETRIC MEASURABLES

In order to quantify the transformation of the $n = 1$ subring shape with spin and inclination, we next choose and calculate geometry-characterizing statistics (“geometric measurables”) on the extracted peak flux locations. For the purposes of training a machine learning algorithm, we seek to identify the smallest set of geometric measurables that can successfully distinguish between subrings at different spins. Ideally, these measurables will be computable in $\mathcal{O}(n)$ (linear) or $\mathcal{O}(n \log n)$ (logarithmic) time complexity, to minimize the time required to generate training data. Additionally, these measurables cannot be constructed in reference to any absolute coordinate system, as an absolute phase reference will likely be unavailable to BHEX.

The shape of the $n = 1$ subring is well-approximated by an ellipse for a large majority of the a - θ_0 parameter space. An ellipse fit encodes useful information, but the iterative nature of any objective function minimization routine makes

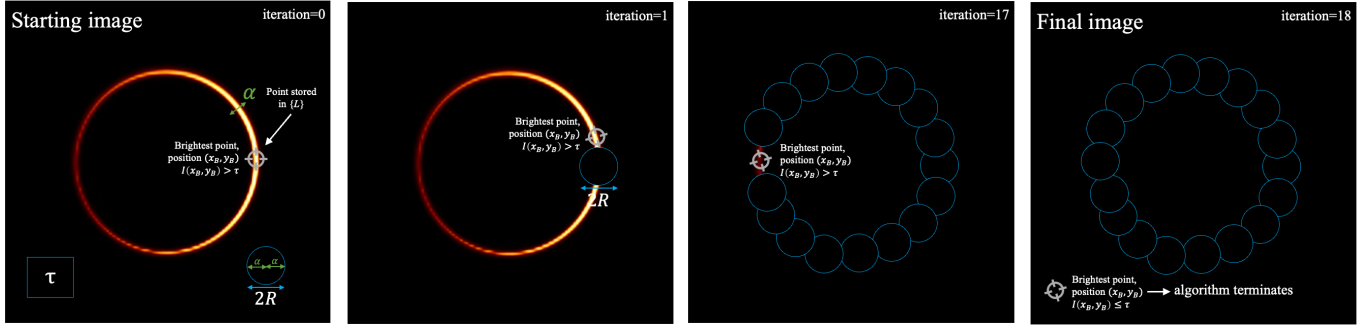


Figure 2. Visualization of the recursive brightest-point (RBP) extraction algorithm. The starting image configuration (far left) is used to estimate acceptable values for the algorithm parameters. The masking radius \mathcal{R} is set to some value greater than the average radial emission profile width α . The noise stopping criterion τ is estimated based on a 5σ upper limit on the background flux distribution, sampled from within the blue square region. For the zeroth iteration, the brightest point, at position (x_B, y_B) is found and added to $\{\mathcal{L}\}$. A region of radius \mathcal{R} is masked out centered on (x_B, y_B) , and the masked image is recursively passed to the algorithm. For the next iteration, the next brightest point is found and added to $\{\mathcal{L}\}$, and the masking is repeated. This process is repeated for 17 iterations (middle right), during which the final point on the ring is masked out. On the final iteration (far right), all meaningful emission from the $n = 1$ photon ring has been masked out and the only flux left is noise. The brightest point in the image now has an intensity less than our stopping criterion τ , so the algorithm terminates.

a fit sub-optimal for performance. As an alternative, we use the *smallest enclosing ellipse* (SEE), the ellipse of smallest area which encloses all recovered points. The SEE can be calculated recursively in $\mathcal{O}(n)$ time (Gartner & Sven 1997). Additionally, the SEE has a much higher degree of variation with spin than a corresponding ellipse fit, making it a more effective diagnostic. This higher degree of variation is caused by the SEE encoding information about the brightness modulation around the ring, but also makes the SEE diagnostic more sensitive to the dynamic range of the interferometer. To construct our geometric measurables, we define the following quantities: r_a , the semimajor axis of the SEE; r_b , the semiminor axis of the SEE; φ_S , the principal angle of the SEE; and $\mathbf{C}_S = (x_{ab}, y_{ab})$, the centroid of the SEE. We additionally construct the center-of-mass \mathbf{C}_m of the peak flux locations $\{\mathcal{L}\}_{i=0}^N$ with

$$\mathbf{C}_m = \begin{bmatrix} C_x \\ C_y \end{bmatrix} = \begin{bmatrix} \frac{1}{N} \sum_i L_i^x \\ \frac{1}{N} \sum_i L_i^y \end{bmatrix}, \quad (1)$$

where L_i^x denotes the x component of a point identified by the RBP algorithm. We propose the following geometric measurables to comply with the constraints discussed above:

1. ε : an eccentricity parameter, constructed via

$$\varepsilon \equiv \frac{1}{r_a} \sqrt{r_a^2 - r_b^2},$$
2. $|\mathbf{C}_m - \mathbf{C}_S|/r_a$: Magnitude of vector between SEE centroid and center-of-mass of points, and
3. $\varphi_S - \arg(\mathbf{C}_m - \mathbf{C}_S)$: Angle of SEE relative to vector between centroid and center-of-mass of points.

These geometric measurables can be computed with linear time complexity, and are generally non-redundant, making them ideal for both generating and fitting our 10^6 element

training set. Critically, these measurables are also scaled to a proxy of the overall size of the subring image (r_a), making them insensitive to the M/D ratio or the emission radius of the target black hole. In addition to these measurables, we also fit an ellipse with semimajor axis a_e , semiminor axis b_e , and principal angle φ_e to the peak flux locations $\{\mathcal{L}\}$ for the purpose of characterizing the $n = 1$ subring shape independent of the brightness modulation. These quantities (a_e, b_e, φ_e) are not used for training, and are computed for a smaller ($\sim 3 \times 10^4$) grid of images spanning the a - θ_0 parameter space for comparison to the SEE measurables.

4.1. Numerical variation with black hole properties

We compute each of the quantities described above for the images in our dataset and plot a heatmap of each result in Figure 3. Broadly, all geometric measurables show relatively smooth and simple behavior modification with spin and inclination. At inclinations below $\theta_0 \approx 40^\circ$, much of the geometric behavior of the rings is highly degenerate, indicating likely significant challenges distinguishing spin at low inclination (such as that of M87*). Most parameters tend to an extreme value in the limit of high spin and edge-on inclination, except for the vertical component of $|\mathbf{C}_m - \mathbf{C}_S|$, which becomes most extreme towards low spin and high inclination. After the $\theta_0 \gtrsim 40^\circ$ boundary, variation in the parameters is fairly linear up to maximum spin and edge-on inclination. In general, all parameters varied substantially more for negative spins than for positive spins.

The ellipse semimajor and semiminor axes as well as the orientation show substantially less variation across the Kerr parameter space. In contrast to the SEE parameters, the size parameters of the ellipse fit vary $\lesssim 6\%$ as spin and inclination are modified. In general, the lower variation makes spin predictions based solely on ellipse fits significantly less discriminatory than predictions based on the SEE model, or a similar model which incorporates brightness distribution.

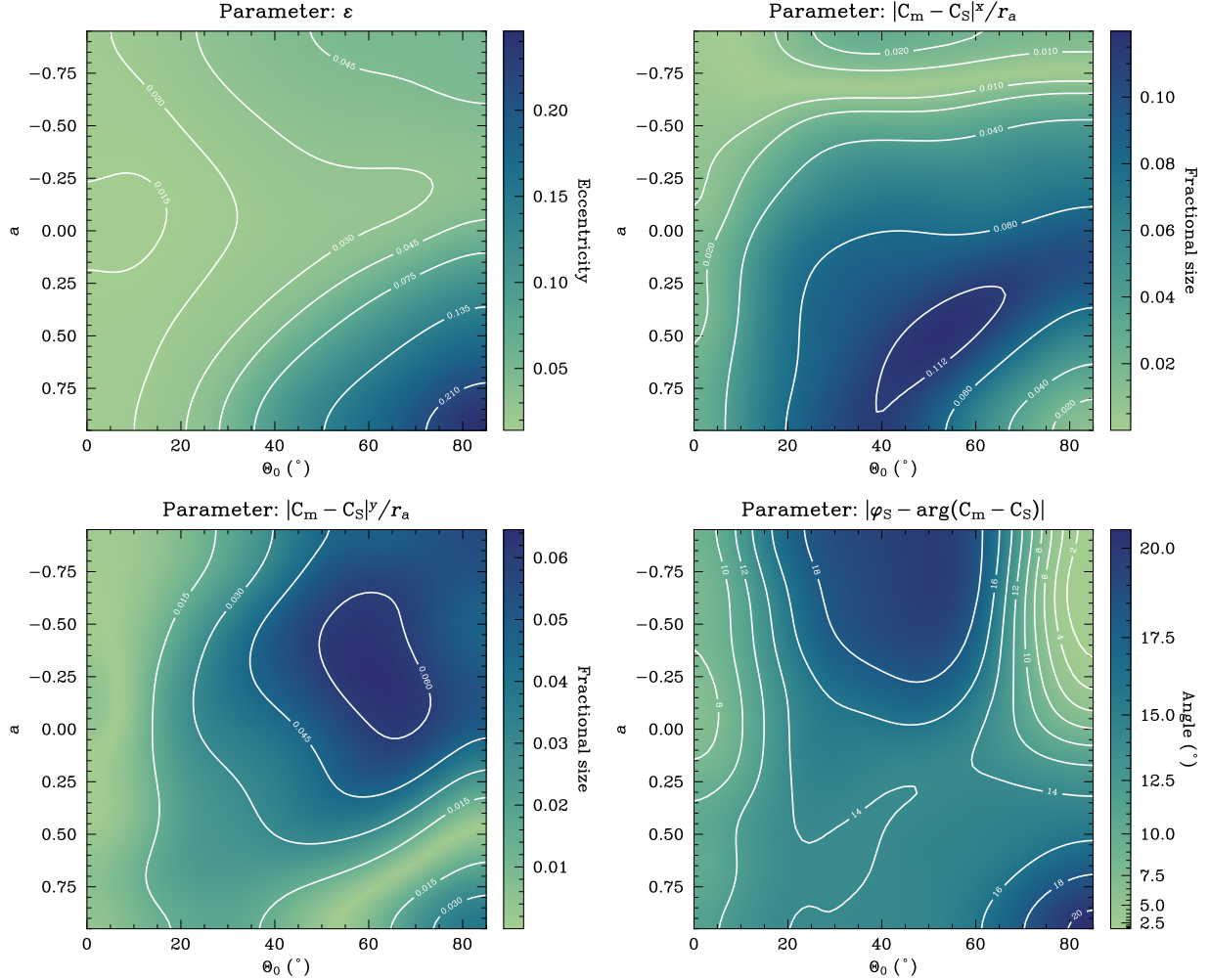


Figure 3. Heatmaps of the SEE quantities described in Section 4.

The variation for all SEE parameters is more easily characterized by considering only positive or negative spin. To this end, we present approximate formulae for the variation of the geometric measurables with spin and inclination. We fit a third-order bivariate polynomial (BV) Q in a and θ_0 to an arbitrary quantity $Q(a, \theta_0)$ using the following expression:

$$Q = \sum_{i,j=0}^3 A_{i,j} a^i \theta_0^j, \quad (2)$$

where $\{A_{i,j}\}$ are the fit coefficients. These fits are performed separately for positive and negative spins. We perform a least-squares minimization over the heatmap distributions in Figure 3 using this function and use the best-fit bivariate polynomial to approximate the behavior of the $n = 1$ photon ring morphology. An example visualization of the fit to the r_b parameter of the SEE model is shown in Figure 4. We present BV parameters for all SEE model parameters in Table 2 and Table 3. On average, we find an average residual of $\lesssim 2\%$ across all spins and inclinations, which indicates excellent fits for all parameters.

5. MACHINE LEARNING APPLICATION

Recent advancements in machine learning have revolutionized various scientific domains, including astrophysics, by enabling the development of sophisticated data analysis techniques. Among these, gradient boosting and convolutional neural networks (CNNs) have emerged as particularly impactful. Gradient boosting Friedman (2001); Chen & Guestrin (2016) has proven effective for structured data analysis, offering robust predictive performance through the ensemble of weak learners. Concurrently, CNNs (Lecun et al. 1998; Krizhevsky et al. 2012) have significantly advanced computer vision tasks, providing powerful tools for image recognition and classification. Here, we apply these techniques to the study of the $n = 1$ photon ring. In Subsection 5.4, we implement a convolutional neural network following the Bayesian neural network in van der Gucht et al. (2020) to estimate spin a directly from images of the $n = 1$ photon ring. In addition, we attempt to approximate the anticipated performance of such a neural network by training a gradient boosting regression model on the geometric measurables presented in Section 4.

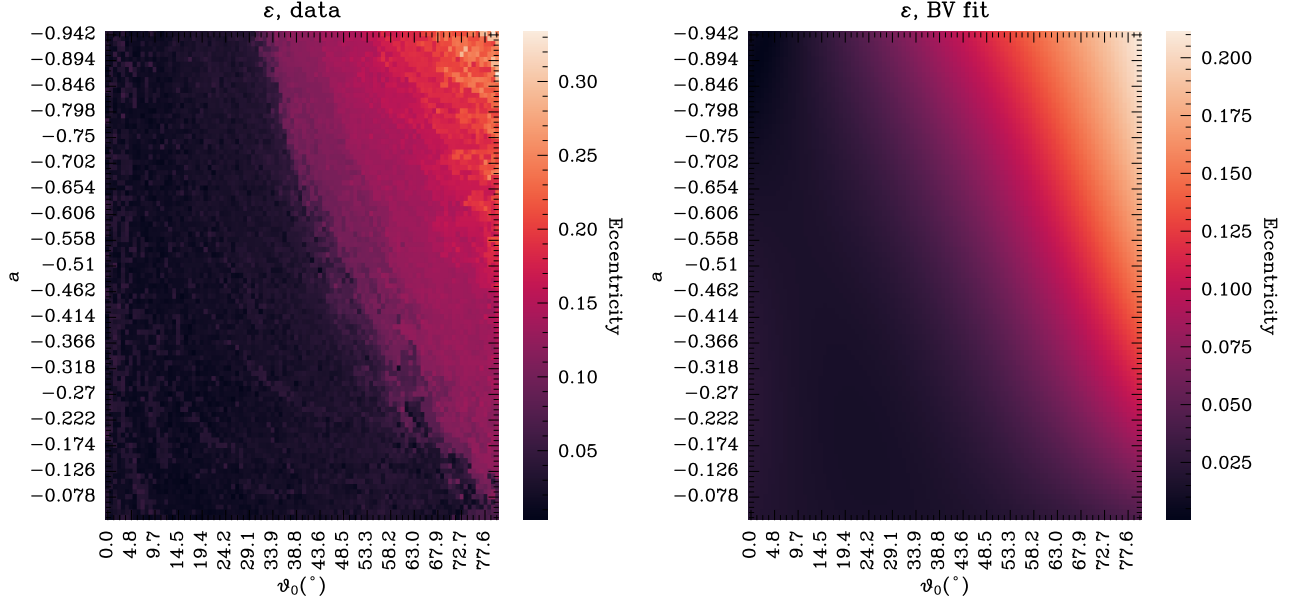


Figure 4. Example visualization of the fits to the SEE and ellipse parameters using a third-order bivariate polynomial (BV). (*left*) The best-fit values of r_b for every combination of spin and inclination in the dataset. (*right*) A description of the r_b parameter using a third-order BV fit. The fit has an average residual of $\lesssim 2\%$, indicating a good fit.

$a < 0$

Parameter	A_{00}	A_{01}	A_{02}	A_{10}	A_{11}	A_{12}	A_{20}	A_{21}	A_{22}
ε	0.206	-0.008	1.0×10^{-4}	-0.002	0.023	-7.6×10^{-4}	-0.412	0.065	-0.001
$ \mathbf{C}_m - \mathbf{C}_S ^x / r_a$	-0.062	0.006	-9.3×10^{-5}	-0.338	0.031	-3.5×10^{-4}	-0.248	0.019	-1.8×10^{-4}
$ \mathbf{C}_m - \mathbf{C}_S ^y / r_a$	-0.008	5.5×10^{-4}	-2.0×10^{-5}	-0.081	0.010	-1.5×10^{-4}	-0.080	0.010	-1.2×10^{-4}
$\varphi_S - \arg(\mathbf{C}_m - \mathbf{C}_S)$	0.796	-3.400	0.036	150.000	-8.830	0.123	133.000	-8.790	0.123

Table 2. BV fit values for the A_{ij} matrix components for negative spin ($a < 0$), computed for each SEE model parameter, as constructed in Section 4.

$a > 0$

Parameter	A_{00}	A_{01}	A_{02}	A_{10}	A_{11}	A_{12}	A_{20}	A_{21}	A_{22}
ε	0.011	2.5×10^{-4}	-8.1×10^{-7}	-0.002	2.8×10^{-4}	1.0×10^{-6}	0.006	5.4×10^{-4}	-7.1×10^{-6}
shfitx	8.0×10^{-4}	-0.003	3.2×10^{-5}	0.004	0.002	-4.3×10^{-5}	-0.019	0.004	-1.6×10^{-5}
shifty	0.014	8.0×10^{-4}	-9.2×10^{-7}	-0.055	0.007	-9.3×10^{-5}	0.059	-0.008	1.1×10^{-4}
alpha	-23.700	-3.610	0.044	24.100	-6.140	0.097	-10.200	3.660	-0.061

Table 3. BV fit values for the A_{ij} matrix components for positive spin ($a > 0$), computed for each SEE model parameter, as constructed in Section 4.

5.1. Setup and training

We implement a gradient boosting regression tree (GBRT) in `scikit-learn` following the notation of [Pedregosa et al. \(2011\)](#) and the references therein in order to estimate spin from the geometric measurables presented in [Section 4](#). We briefly summarize the techniques used here. Gradient boosting is a machine learning technique that incrementally builds an ensemble of weak predictive models, typically decision trees, to optimize performance by minimizing a loss function through iterative improvements. A GBRT regressor constructs a prediction \hat{y}_i for a given input x_i by adding the predictions of a series of M weak “learners” $h_m x_i$; i.e.,

$$\hat{y}_i = \sum_{m=1}^M h_m(x_i). \quad (3)$$

Each estimator h_m is a decision tree regressor of fixed size, constructed to minimize the losses of the summed previous $m - 1$ estimators. The initial estimator h_0 is arbitrary and, for a least-squares loss function, is typically chosen as the mean of the response variables. The parameters of the trees are fit via a functional space gradient descent.

We implement the `GradientBoostingRegressor` in `scikit-learn` initialized with $M = 125$ and a least-squares loss function. The value of M was chosen based on performance on the validation set. As M increases, the performance of the network asymptotically approaches some maximum accuracy, and can even decrease as overfitting effects increase. We choose the number of learners M such that the accuracy achieves $\approx 99\%$ of the maximum, to maximize performance while avoiding overfitting. We train on the input quantities $(r_a, r_b, |\mathbf{C}_m - \mathbf{C}_S|, \varphi_S - \arg(\mathbf{C}_m - \mathbf{C}_S))$ described in [Section 4](#) and response variable spin (a). We train on 90% of the full (10^6 images) dataset, separating 10% (10^5 images) of the dataset as a universal validation dataset (which the network never sees) to prevent overfitting. For testing purposes, we also attempted training with 95% and 80% of the full dataset (with 5% and 20% of the dataset for validation, respectively) and did not notice a significant variation ($\lesssim 1\%$) in the performance of the algorithm. The raw prediction of the algorithm \hat{y}_i is treated as the spin estimate with no modifications.

We next estimate an uncertainty on our measurement. Broadly, there are two types of estimate uncertainties: *epistemic* uncertainties, capturing the insufficiency of the model; and *aleatoric* uncertainties, which capture the intrinsic uncertainty present in the data. We discuss both below.

To estimate an epistemic uncertainty, we implement cross-validation similar to the stochastic gradient boosting technique ([Friedman 2002](#)). In addition to the main prediction algorithm, we perform 10 leave-one-out bootstrapping steps, which we refer to as “bootstrap samples”. Each training set of these samples is randomly selected to be 40% of the whole dataset, with the remaining 10% used as the validation set. After an estimate of spin is made by using the whole dataset for a prediction, the samples are similarly queried to produce a range of predictions $\{\hat{y}_k\}_{k=0}^{10}$ based on their limited sample

of the dataset. The standard deviation of this range $\sigma_{\hat{y},k}$ is used as an estimate of the epistemic uncertainty. The purpose of this uncertainty is to estimate how sensitive our prediction is to the particular construction of the dataset and choice of input images.

To estimate an aleatoric uncertainty, we consider the largest source of uncertainty in an estimate of spin: namely, the degeneracy of the photon ring shape as the inclination varies. At low inclination, the geometric shape of the photon ring is virtually invariant to spin. The degeneracies are visible in [Figure 3](#), where most parameters see little-to-no variation at inclinations $\theta_0 \lesssim 40^\circ$. To quantify the uncertainty due to this degeneracy, for each spin a we consider a range of inclinations $[\theta_0, \theta_0 + \delta\theta_0]$. Within this range, we adopt the standard deviation σ_{θ_0} of the estimates of spin for each (a, θ_0) combination as an estimate of the aleatoric uncertainty resulting from the inclination degeneracy. We choose $\delta\theta_0 = 19.75^\circ$, corresponding to 25% of the inclination range we generated for the dataset. Each bin of inclination would therefore contain $\approx 2.5 \times 10^3$ spin estimates at that inclination range, making it an effective approximation of the estimate variance due to the inclination degeneracy.

We add together our aleatoric and epistemic uncertainties together in quadrature to construct a global uncertainty estimate. In general, we found that $\sigma_{\hat{y},k} \ll \sigma_{\theta_0}$, making the inclination degeneracy the dominant source of uncertainty in our estimates.

5.2. Overall performance of the GBRT

We consider the overall performance of the GBRT described in [Subsection 5.1](#) with and without convolution, and with retraining. The maximum nominal BHEX beam is expected to be $\approx 9 \mu\text{as}$, corresponding to operations at 230 GHz, and resulting in an imaging resolution of $\approx 4.5 \mu\text{as}$. At 345 GHz, the BHEX beam is expected to be $\approx 6 \mu\text{as}$, corresponding to an imaging resolution of $\approx 3 \mu\text{as}$. Thus, to conservatively simulate BHEX imaging conditions, we test the performance of the GBRT under a convolution of $6 \mu\text{as}$, with and without retraining. The distribution of residuals between the predicted and estimated spins is shown in [Figure 5](#). We find an average residual of ≈ 0 ($r^2 \approx 0.95$) with a spread of $\lesssim \pm 0.2$ on the unconvolved dataset. This corresponds to $\lesssim 20\%$ of the full range of spins and is convincing evidence that, in the absence of noise and other artifacts, the photon ring geometry and brightness distribution is sufficient to distinguish between different spins. The performance is significantly worsened after convolution with a $6\mu\text{as}$ beam. At this convolution, the average residual is still ≈ 0 ; however, the spread of deviations is 2-3x larger than the spread of deviations with no convolution. Additionally, there is a skew towards negative values of $a_{\text{estimated}} - a_{\text{truth}}$, indicating that the effect of convolution on our pipeline is an underestimate of spin for a significant portion of the dataset.

5.3. Intra-inclination performance of the GBRT

We now consider the performance of the GBRT at different inclinations. Due to the inclination degeneracy, we

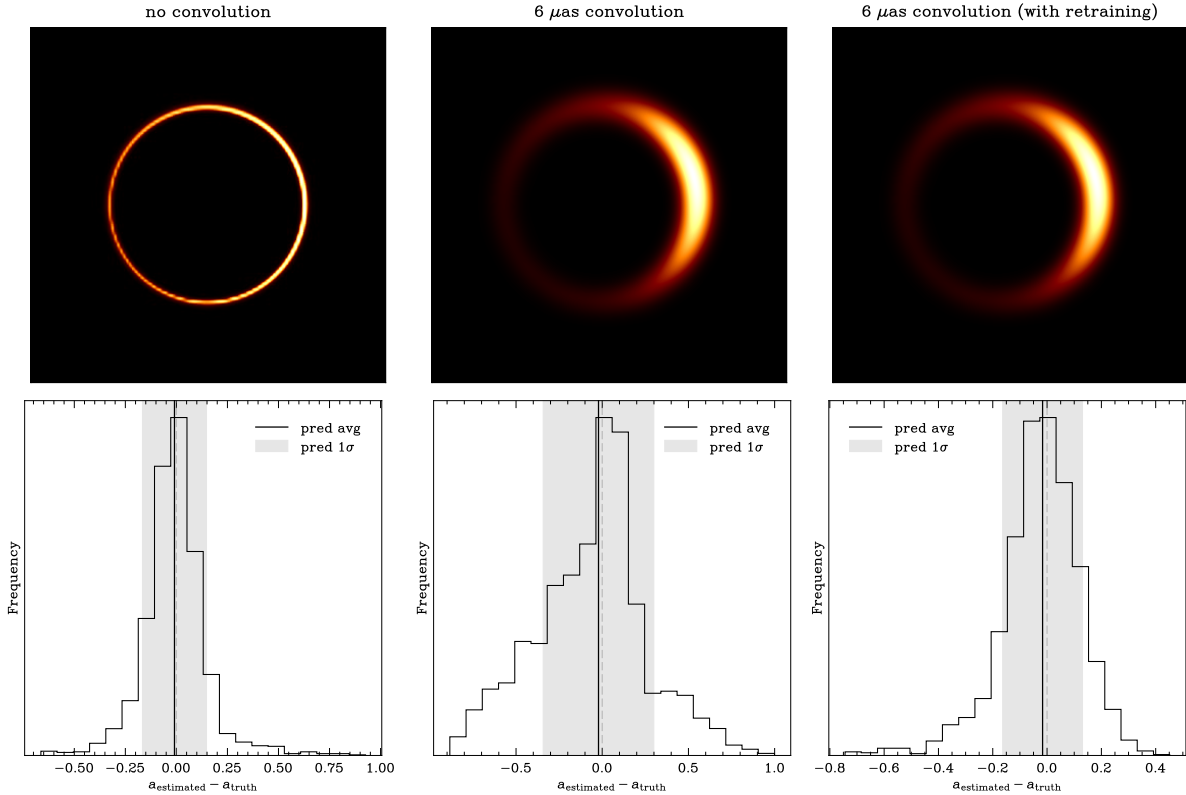


Figure 5. Performance at varying convolution for the GBRT described in [Subsection 5.1](#). (*top*) Representative appearances of the $n = 1$ photon ring at varying convolutions, ranging from no convolution (left) to the anticipated BHEX beam at 345 GHz (center and right). (*bottom*) Performance of the GBRT with the convolution level shown in the top row. With no convolution, or convolution with retraining, recovery is highly accurate. As the size of the convolving beam is increased, the performance of the network without retraining predictably deteriorates.

expect variable performance of the neural network as inclination is varied. In [Figure 6](#), we visualize the performance of the GBRT on four inclination ranges: face-on (0° to 20°), low (20° to 40°), high (40° to 60°), and edge-on (60° to 90°). We perform this visualization for the GBRT trained on non-convolved data operating on non-convolved data, as well as the equivalent analysis for the GBRT operating on data convolved with a $6 \mu\text{as}$ beam. Unexpectedly, we find that GBRT performance at low and face-on inclinations in the non-convolved case is similar to the performance at high and edge-on inclinations. Recovery at all inclinations is consistent (within the aleatoric uncertainty) with perfect recovery, although there is a systematic under-estimation of the spin magnitude of $\lesssim 5\%$ (of the full spin range) at spins with $a < -0.8$ for $\theta_0 \in [40^\circ, 60^\circ]$. The other inclination ranges show comparable performance. The excellent performance even at low spins and inclinations indicates that, in the absence of imaging convolution and artifacts, the $n = 1$ photon ring can be a distinguishing proxy for spin.

The network performance is significantly worsened when realistic BHEX convolution is introduced in images. When images are convolved with a $6 \mu\text{as}$ beam (no retraining), negative spins are recovered accurately (though with a significantly larger spread in predictions). However, positive spins are largely under-estimated, with most estimates being

consistent with $a = 0$. When the network is retrained on images convolved with the $6 \mu\text{as}$ BHEX beam, the performance is comparable to the $0 \mu\text{as}$ convolution test at inclinations $\theta_0 > 20^\circ$. At inclinations $\theta_0 < 20^\circ$, estimates are still consistent with the true values, but there is a greater tendency to underestimate the spin magnitude.

The lower performance with convolution indicates that an image feature-extraction approach may be inadequate to perform spin extraction using the $n = 1$ photon ring unless estimation tools are trained specifically at the anticipated BHEX resolution. However, the excellent performance with no convolution indicates that the $n = 1$ photon ring can be a distinguishing proxy for spin in the absence of convolution or imaging artifacts. Performing spin estimates using Fourier analogs of the geometric measurables may sidestep confounding effects from imaging; we investigate this method of spin inference in [Farah et al. \(2024ip\)](#).

5.4. Comparison to Deep Horizon

Convolutional neural networks (CNNs) and the cousin Bayesian neural networks (BNNs) have been used in past analyses to demonstrate recovery of simulation parameters from GRMHD simulations of black hole accretion flows ([van der Gucht et al. 2020](#)). The primary benefit of a CNN is the ability to train on and input entire images, without needing

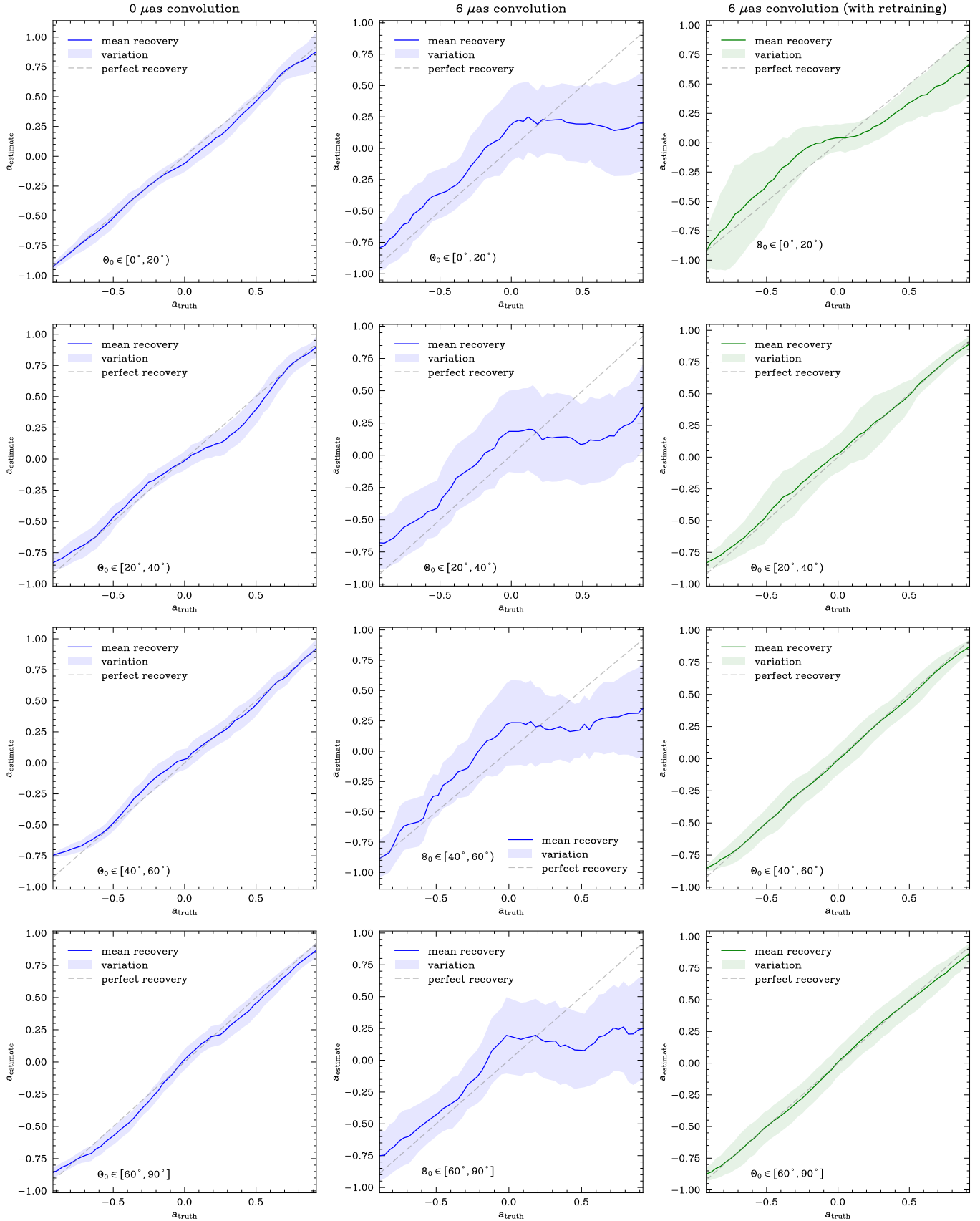


Figure 6. Intra-inclination performance of the GBRT on four inclination ranges: face-on (0° to 20°), low (20° to 40°), high (40° to 60°), and edge-on (60° to 90°). The left column (blue) corresponds to the GBRT trained on non-convolved data operating on non-convolved data; the right column (green) is the equivalent analysis for the GBRT operating on data convolved with the $6 \mu\text{s}$ beam. The center column corresponds to the GBRT trained on non-convolved data operating on data convolved with a $6 \mu\text{s}$ BHEX beam. The shaded region in all plots corresponds to the aleatoric uncertainty σ_{θ_0} computed in [Subsection 5.1](#).

to perform feature extraction or calculate geometric measurables. This feature of CNNs practically guarantees that they will outperform alternative machine learning algorithms such as GBRT. However, CNNs are also slow to train as a result of running on full, often high-resolution images. By implementing a CNN and comparing the performance to our GBRT, we can assess how effectively our choice of geometric measurables is utilizing the information present in the images.

We reproduce the methodology of [van der Gucht et al. \(2020\)](#) with minor modifications. We implement a CNN in TensorFlow version 2.14 ([Abadi et al. 2015](#)) leveraging the keras ([Chollet et al. 2015](#)) API version 2.14. We choose and implement a 10-layer CNN architecture. Following [van der Gucht et al. \(2020\)](#), we use a rectified linear unit activation function ([Nair & Hinton 2010](#)) for all layers except the output layer. We use 90% of the full dataset for training and separate the remaining 10% for validation. The network is trained on the input data using the legacy implementation of the Adam optimizer ([Kingma & Ba 2015](#)). The network is initialized with the mean squared error as the primary loss function, with the mean absolute error as an evaluation metric. We use a fixed learning rate of 0.001 for all implementations and runs.

We apply the network architecture and training pipeline to both non-convolved images and images convolved with the BHEX beam. The results are shown in [Figure 7](#) and [Figure 8](#). The performance on non-convolved images is almost identical to the performance for the corresponding GBRT, featuring a mean residual of ≈ 0 and a $\lesssim 20\%$ improvement in the residual spread. We follow [van der Gucht et al. \(2020\)](#) and also visualize the performance via a scatter plot of spin recoveries, color-coded by standard deviations from perfect recovery. The network reports consistently accurate recovery of spin at all spin and inclination combinations, with marginally worse performance below $a \lesssim 0.2$. The similarity of the performance between the CNN and the GBRT is a strong validation in the choice of geometric measurables being sufficient to capture the salient and spin-distinguishing features of the $n = 1$ photon ring. However, the CNN drastically outperforms the GBRT on images convolved with the BHEX beam, indicating the GBRT may not be fully suitable for direct application to BHEX images.

6. APPLICATION TO GRMHD SIMULATIONS

The analysis previously discussed in this work was based on the semi-analytic simulation engine KerrBAM. Here, we apply the methods developed using KerrBAM to GRMHD simulations of black hole accretion flows. The purpose of this analysis is to provide validation that methods developed using semi-analytic simulation engines can be applied to complex simulations more analogous to a real black hole environment. Additionally, full numerical GRMHD simulations were not included in the training for either the GBRT or CNN networks, making a test on GRMHD simulations a more challenging evaluation of network performance.

6.1. Preparation of synthetic data

We analyze the decomposed sub-images from the model set ray-traced in [Palumbo & Wong \(2022\)](#). These simulations have a mass-to-distance ratio corresponding to the EHT estimate for M87*. The fluid models were simulated with `iharm3D` ([Gammie et al. 2003](#); [Prather et al. 2021](#)) and ray traced with `ipole` ([Mościbrodzka & Gammie 2018](#)), using the $R_{\text{high}} = 40$ electron heating parameter described in [Mościbrodzka et al. \(2016\)](#). More details about the GRMHD and General Relativistic Ray Tracing (GRRT) pipeline can be found in [Wong et al. \(2022\)](#). The resulting images are time-averaged to produce smooth images of typical accretion flow structures, including the photon ring. We generate three GRMHD simulations at $a = 0.0, -0.5$ and -0.94 . The inclinations are generated at the expected inclination angle for M87* ($\theta_0 \approx 17^\circ$).

6.2. Application to $n = 1$ GRMHD simulations

We apply the two algorithms discussed previously (GBRT and CNN) to the GRMHD simulations constructed [Subsection 6.1](#). For the GBRT, we measure the geometric observables constructed in [Section 4](#) and pass them into the GBRT, which returns an estimate of the spin. For the CNN, we simply resize the image to the 128x128px input size and pass it into the CNN, which returns an estimate of the spin. The results are shown in [Figure 9](#). Performance between the two approaches is very similar, despite the difference in method. The similarities in performance on GRMHD are an additional validation that the geometric measurables constructed in [Section 4](#) capture most, if not all, of the salient features distinguishing spin. Both methods recovery spin values consistent with the ground truth simulation at $|a| \gtrsim 0.5$, but overestimate the low spin simulations in a manner consistent with complications from the spin-inclination degeneracy problem. Performance could be improved by breaking this degeneracy; future methods may incorporate information from e.g., polarization, which is modified by frame-dragging but is also heavily influenced by properties of the plasma flow in the vicinity ([Akiyama et al. 2017](#); [Event Horizon Telescope Collaboration 2021a](#); [Palumbo & Wong 2022](#)); or constraints on the diameter measured in Fourier space, known to vary tightly with spin ([Johnson et al. 2020](#); [Lupsasca et al. 2024b](#); [Farah et al. 2024ip](#)).

The accuracy of the spin recovery on both the KerrBAM and GRMHD images is a strong preliminary indication that the $n = 1$ photon ring has utility as a proxy to measure spin, with the essential caveat that these tests have been performed on noiseless images without the contribution of the $n = 0$ and $n > 1$ subring emission. The presence of additional subrings in BHEX images—particularly the $n = 0$ direct emission, which is dominated by surrounding astrophysical effects and not the black hole properties—will likely overwhelm the $n = 1$ photon ring emission, making the image-domain approach described here potentially infeasible for precise spin measurements.

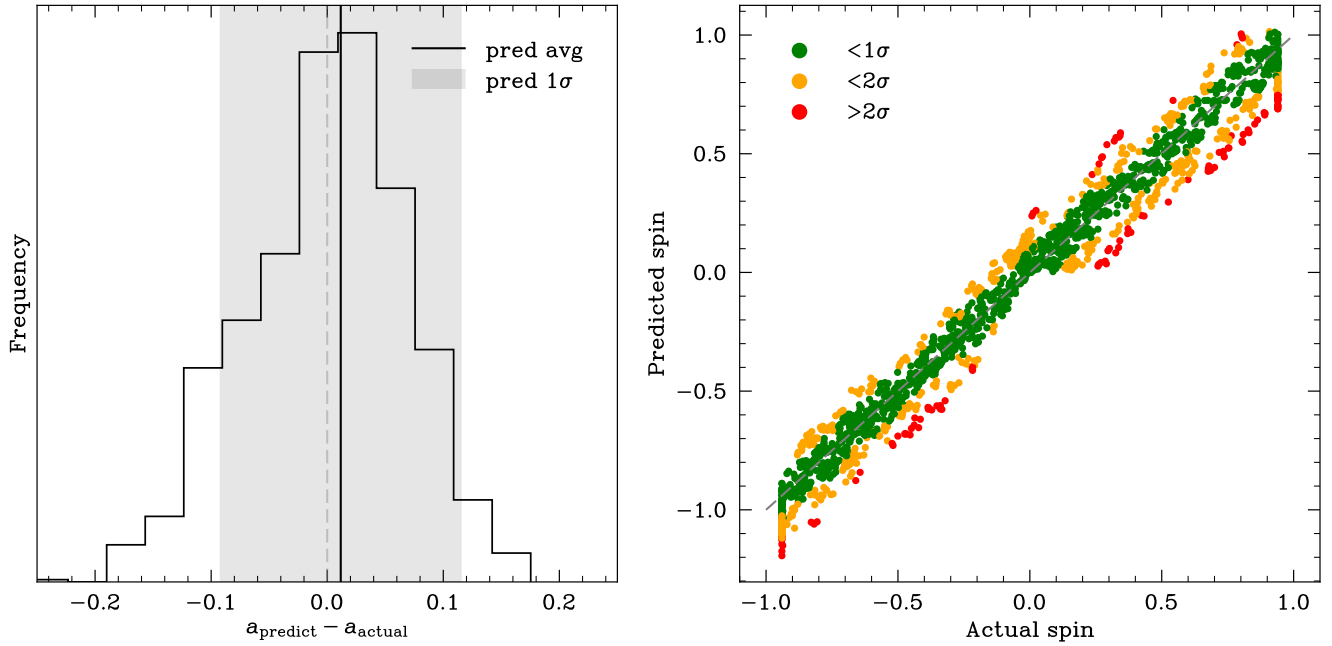


Figure 7. Performance of a CNN trained on non-convolved images. We find recovery performance approximately comparable to the performance of the GBRT. The left histogram is an aggregation of recovery residuals, showing an average residual close to zero with a narrow spread of $\lesssim 0.1$. The scatterplot on the right shows sample recoveries at all spins, color-coded by the deviation from the mean recovery at a particular spin.

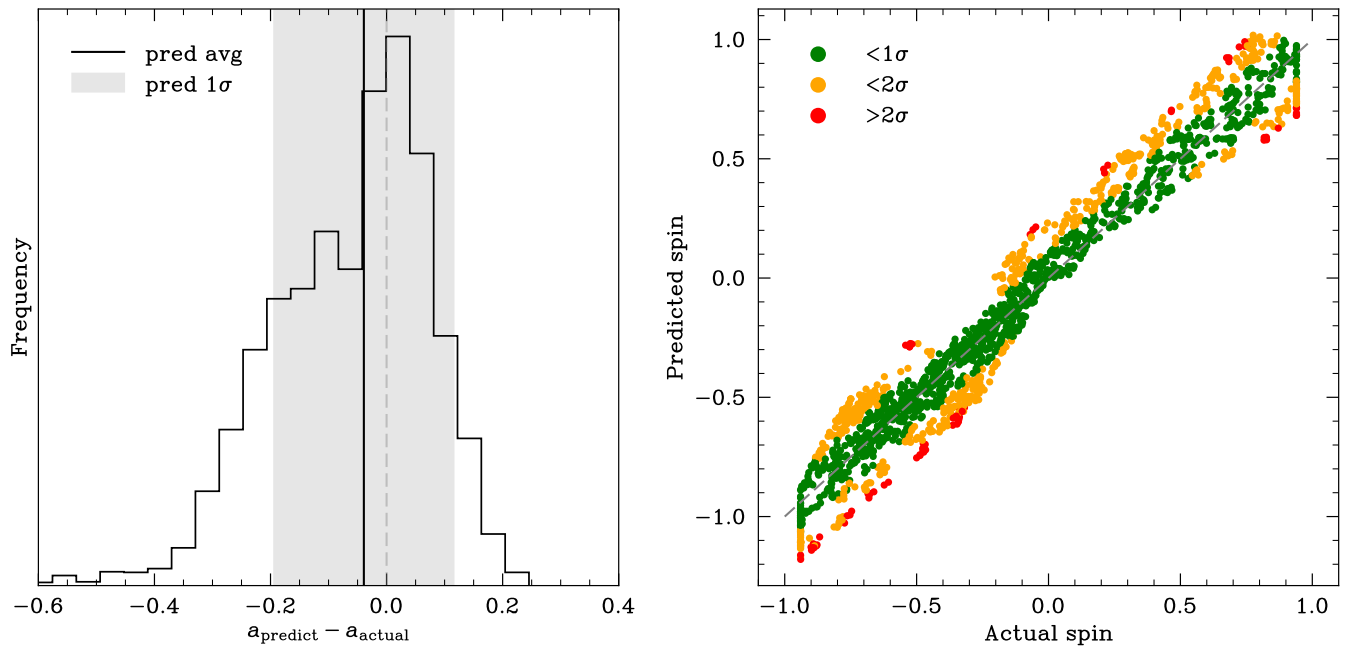


Figure 8. Same as Figure 7, but for a CNN operating on images convolved with the nominal BHEX beam ($6\mu\text{as}$, bottom), without retraining. We find recovery performance approximately comparable to the performance of the GBRT and the non-convolved network.

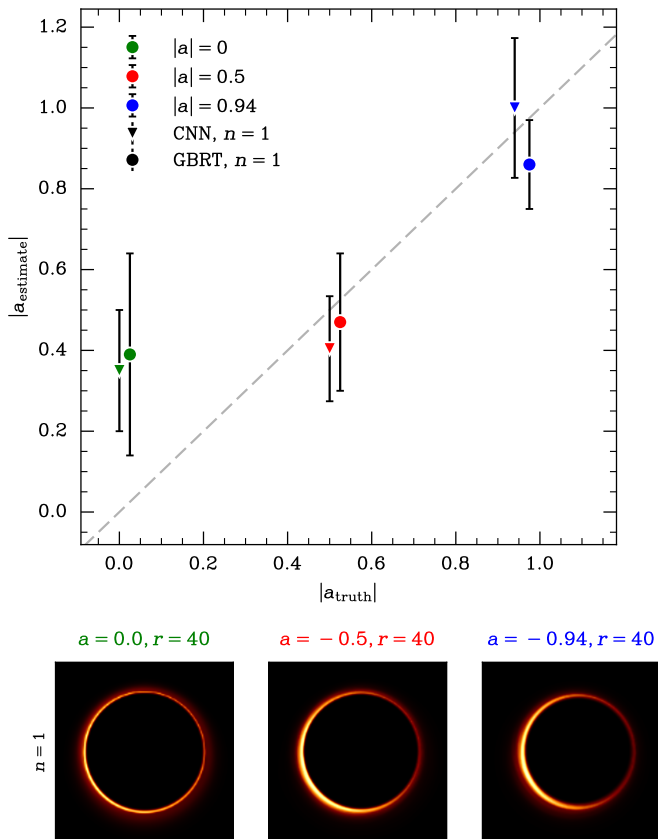


Figure 9. (top) Performance of the GRBT (circle points) and CNN (triangle points) on GRMHD images generated following the description in Subsection 6.1. The two approaches report very similar performance on GRMHD simulations. Recovery of spin is excellent, despite the low inclination and despite neither using GRMHD images in their training data. Perfect recovery is shown with the gray dashed line. Note: the $|a_{\text{truth}}|$ values are offset by ± 0.025 to improve clarity; the true spin values were either 0.0, -0.5 , or -0.94 . (bottom) The simulated images $n = 1$ passed into the GBRT and CNN.

7. CONCLUSIONS

The upcoming BHEX orbiting observation platform will enable an unprecedented view of the photon rings of the largest black holes on the sky. In particular, BHEX will probe the $n = 1$ subring, which is largely invariant to surrounding astrophysical phenomenon and primarily affected by the black hole’s spin and inclination. As a result, the $n = 1$ photon ring has the potential to serve as a proxy for precisely measuring the spin of the black hole. However, the behavior of the $n = 1$ subring as spin is varied is not completely understood, presenting a potential obstacle for tools hoping to exploit it to measure angular momentum.

We present an end-to-end pipeline for characterizing the variation of black hole subrings as the properties of the black hole is modified. We take advantage of the fast semi-analytic simulation engine *KerrBAM* to generate a large vol-

ume ($\gtrsim 10^6$) of $n = 1$ subrings, varying spin and inclination in small increments. We develop a novel feature extraction algorithm (recursive brightest-point extraction) that is capable of extracting the non-circular brightness profiles of the subrings from these images on a short timescale, representing a $\sim 10^3$ x performance increase over existing EHT-based tools. Next, we construct a series of geometric measurables which characterize the shape, orientation, and brightness distribution of the emission profile, and construct a large training set from these quantities.

Our large dataset of $n = 1$ subrings, combined with the minimal set of descriptive observables, provides an opportunity to precisely characterize the behavior of the $n = 1$ subring. We quantify the behavior by fitting a bivariate cubic polynomial to each quantity and provide a mapping between combinations of (a, θ_0) and each geometric measurable. We then develop and apply a gradient boosted regression tree (GBRT) to the dataset of geometric measurables to broadly test whether these measurables are sufficient to constrain spin. We additionally test the performance of the GBRT against a convolutional neural network (CNN), which theoretically represents the maximum performance achievable on the images in our dataset (as the image necessarily contains more data than any set of geometric measurables). We find that, under no convolution, the GBRT and CNN are both able to measure spin from images with a high accuracy ($< 10\%$ deviation from truth spin for all spins and inclinations). However, when convolution up to the BHEX beam ($\approx 10\mu\text{as}$) is introduced, both algorithms suffer at low spin and particularly low inclination, where the photon rings appear highly degenerate. Overall, the GBRT performs remarkably similarly to the CNN, indicating that the geometric measurables we have chosen successfully capture the salient features of the images.

To more fully test the ability of the spin extraction methods described above, we test recovery on GRMHD simulations of black holes. These simulations are typically more accurate to reality but also more computationally expensive to generate. We chose simulations at the M87* inclination of $\theta_0 = 17^\circ$, which was particularly challenging for our algorithms during validation on the *KerrBAM* data. We begin by testing the GBRT and CNN algorithms on GRMHD simulations of the $n = 1$ emission, to probe the utility of training on faster but potentially less accurate semi-analytic models. Remarkably, we find recovery of spin from the GRMHD images to be comparable in accuracy to the *KerrBAM* counterpart tests. Both the CNN and GBRT perform better at high spin and over-estimate the truth values at low spin.

We have presented a comprehensive pipeline for the study and analysis of black hole photon subrings. Analysis of the $n = 1$ subring has illuminated aspects of how its geometry is modified with spin and inclination across the Kerr parameter space. Additionally, we have developed and trained several tools for extracting spin from semi-analytic and GRMHD simulations. Future research can expand upon any of these approaches in order to maximize utility to BHEX. The machine learning algorithms would benefit from an increased training set over a wider range of parameter combinations (e.g.,

electron heating) to both build more robust spin estimates and estimate parameters beyond just spin and inclination. To ensure that these procedures are effective, it is essential to adapt our methods to the specific observational constraints of BHEX. These tools are the basis of viable procedures to measure spin from future, sparse BHEX measurements of target black holes.

We thank the BHEX collaboration for useful discussions and feedback. JF is supported by an NSF-GRFP 2139319. J.D. is supported by a NASA Hubble Fellowship Program Einstein Fellowship. J.D. acknowledges support from a Joint Columbia University and Flatiron Institute Postdoctoral Fellowship. We thank Yaxuan Shen for helpful discussions regarding regularized gradient boosting.

REFERENCES

- Abadi, M., Agarwal, A., Barham, P., & Brevdo. 2015, TensorFlow, Large-scale machine learning on heterogeneous systems
- Akiyama, K., et al. 2017, *AJ*, 153, 159
- Akiyama, K., et al. 2024, arXiv e-prints, arXiv:2406.09516
- Bambi, C., Freese, K., Vagnozzi, S., & Visinelli, L. 2019, *Physical Review D*, 100
- Bardeen, J. 1973, in *Black Holes (Les Astres Occlus)*, ed. C. Dewitt & B. Dewitt (New York), 215–239
- Broderick, A. E., Tiede, P., Pesce, D. W., & Gold, R. 2022, *ApJ*, 927, 6
- Cárdenas-Avendaño, A., Lupsasca, A., & Zhu, H. 2023, *PhRvD*, 107, 043030
- Chael, A. 2024, eht-imaging
- Chen, T., & Guestrin, C. 2016, in *Proceedings of the 22nd ACM SIGKDD International Conference on Knowledge Discovery and Data Mining, KDD '16 (New York, NY, USA: Association for Computing Machinery)*, 785–794
- Chollet, F., et al. 2015, *Keras*, <https://keras.io>
- Cunha, P. V. P., & Herdeiro, C. A. R. 2018, *General Relativity and Gravitation*, 50, 42
- de Vries, A. 2003, *Jahresschrift der Bochumer Interdisziplinären Gesellschaft*
- Event Horizon Telescope Collaboration. 2021a, *ApJL*, 910
- Event Horizon Telescope Collaboration et al. 2019a, 875, L1
- . 2019b, 875, L4
- . 2019c, *The Astrophysical Journal*, 875, L4, (M87 Paper IV)
- . 2019d, 875, L5
- . 2019e, 875, L6
- . 2022a, *The Astrophysical Journal*, 930, L12
- . 2022b, *The Astrophysical Journal*, 930, L14
- . 2022c, *The Astrophysical Journal*, 930, L16
- . 2022d, *The Astrophysical Journal*, 930, L17
- Farah, J. R., Lupsasca, A., Gammie, C., & Quataert, E. 2024ip, *Interferometric inference of black hole spin from the photon ring brightness profile*
- Farah, J. R., Pesce, D. W., Johnson, M. D., & Blackburn, L. 2020, *ApJ*, 900, 77
- Friedman, J. H. 2001, *The Annals of Statistics*, 29, 1189
- . 2002, *Computational Statistics & Data Analysis*, 38, 367, *nonlinear Methods and Data Mining*
- Gammie, C. F., McKinney, J. C., & Tóth, G. 2003, *ApJ*, 589, 444
- Gartner, B., & Sven, S. 1997, *Proceedings of the 13th Annual ACM Symposium on Computational Geometry*
- Gelles, Z., Prather, B. S., Palumbo, D. C. M., Johnson, M. D., Wong, G. N., & Georgiev, B. 2021, *ApJ*, 912, 39
- Gralla, S. E. 2020, *PhRvD*, 102, 044017
- Gralla, S. E., Lupsasca, A., & Marrone, D. P. 2020, *PhRvD*, 102, 124004
- Hastie, T. 2009, *The elements of statistical learning data mining, Inference, and Prediction*
- Johannsen, T., et al. 2016, *PhRvL*, 116, 031101
- Johnson, M. D., et al. 2020, *Science Advances*, 6, eaaz1310
- . 2024, arXiv e-prints, arXiv:2406.12917
- Kingma, D. P., & Ba, J. 2015, in *3rd International Conference on Learning Representations, ICLR 2015, San Diego, CA, USA, May 7-9, 2015, Conference Track Proceedings*, ed. Y. Bengio & Y. LeCun
- Krizhevsky, A., Sutskever, I., & Hinton, G. E. 2012, in *Advances in Neural Information Processing Systems*, ed. F. Pereira, C. Burges, L. Bottou, & K. Weinberger, Vol. 25 (Curran Associates, Inc.)
- Lecun, Y., Bottou, L., Bengio, Y., & Haffner, P. 1998, *Proceedings of the IEEE*, 86, 2278
- Lupsasca, A., Mayerson, D. R., Ripperda, B., & Staelens, S. 2024a, arXiv e-prints, arXiv:2402.01290
- Lupsasca, A., et al. 2024b, arXiv e-prints, arXiv:2406.09498
- Mościbrodzka, M., Falcke, H., & Shiokawa, H. 2016, *A&A*, 586, A38
- Mościbrodzka, M., & Gammie, C. F. 2018, *MNRAS*, 475, 43
- Nair, V., & Hinton, G. E. 2010, in *Proceedings of the 27th International Conference on International Conference on Machine Learning, ICML'10 (Madison, WI, USA: Omnipress)*, 807–814
- Palumbo, D. C. M., Gelles, Z., Tiede, P., Chang, D. O., Pesce, D. W., Chael, A., & Johnson, M. D. 2022, *ApJ*, 939, 107
- Palumbo, D. C. M., & Wong, G. N. 2022, *ApJ*, 929, 49
- Paugnat, H., Lupsasca, A., Vincent, F. H., & Wielgus, M. 2022, *A&A*, 668, A11
- Pedregosa, F., et al. 2011, *Journal of Machine Learning Research*, 12, 2825

Prather, B., Wong, G., Dhruv, V., Ryan, B., Dolence, J., Ressler, S.,
& Gammie, C. 2021, *The Journal of Open Source Software*, 6,
3336
Psaltis, D. 2019, *General Relativity and Gravitation*, 51

van der Gucht, J., Davelaar, J., Hendriks, L., Porth, O., Olivares, H.,
Mizuno, Y., Fromm, C. M., & Falcke, H. 2020, *A&A*, 636, A94
Wong, G. N., et al. 2022, arXiv e-prints, arXiv:2202.11721